WILEY-VCH

DOI: 10.1002/((please add manuscript number))

Article type: Communication

3D-printed mechanical metamaterials with high performance of energy absorption

Shangqin Yuan, Chee Kai Chua, and Kun Zhou*

Singapore Centre for 3D Printing, School of Mechanical and Aerospace Engineering, Nanyang Technological University, Singapore 639798, Singapore

Dr. Shangqin Yuan
School of Mechanical & Aerospace Engineering,
Singapore Centre for 3D Printing
Nanyang Technological University, Singapore 639798

Dr. Chee Kai Chua
Professor, School of Mechanical & Aerospace Engineering,
Executive Director, Singapore Centre for 3D Printing
Nanyang Technological University, Singapore 639798

Dr. Kun Zhou
Associate Professor, School of Mechanical & Aerospace Engineering,
Singapore Centre for 3D Printing
Nanyang Technological University, Singapore 639798
Email: kzhou@ntu.edu.sg

Keywords: additive manufacturing, 3D-printed mechanical metamaterials, energy absorption, selective laser sintering, auxetic composite lattices

Abstract

Recently, three-dimensional (3D) metamaterials have been achieved with the inaccessible mechanical properties in natural materials such as negative Poisson's ratio, stiffness, and thermal expansion coefficient. While most of the developed metamaterials with engineerable structural deformation evolution, few studies have revealed their potential in energy absorption due to the limited mechanical properties of 3D-printed constituent materials and inevitable structural defects induced by the manufacturing process.[1, 2-4] Herein, an approach is proposed for creating 3D metamaterials of auxetic composite lattices via laser-sintering of CNT-reinforced nanocomposites, which provide a platform for the design and manufacturing of systems with programmable energy absorption capability. The optimization of constituent material and structural design enables the improvement of energy absorption performance across multiple scales. The energy absorption capacity of auxetic metamaterials was exponentially scaled with the relative density with the order of 2.5 ~3. The rationally topologized auxetic metamaterials exhibit a combination of high specific densification strength (0.0195 MPa/kg m^3), ultrahigh energy absorption capacity (6.29 MJ/m^3) and excellent special energy absorption (20.42 J/g). Impressively, this group of auxetic metamaterials possesses the advantageous specific energy absorption approaching to titanium alloy foams as well as over a broad range of materials including plastic foams, aluminum alloy foams and other 3D-printed lightweight structures.

Metamaterials are rational artificial materials with unique structural designs to manipulate and control light,[5] sound,[6, 7] mechanical stress,[8, 9] etc., leading to previously inaccessible properties in photonic,[10] acoustic,[6] mechanical,[11, 12] and many other physical aspects. Three-dimensional (3D) auxetic materials with highly-ordered packing are firstly observed in the deformation of metallic crystal.[13] To date, the 3D metamaterials facilitate the combinations of mechanical properties that are in principle antagonistic, such as ultrahigh stiffness, high damping capability, or negative Poisson's ratio.[14-16] These properties are derived both from the geometrical arrangement of those materials, as well as from the inherent properties of their constituent materials. However, the integration of the customized material formulation and rapid 3D structural design across multiple scales are hard to be achieved by classical material development (e.g. chemical synthesis and self-assembly) and conventional manufacturing approaches (e.g. moulding, tooling, and cutting).

By virtue of 3D mechanical metamaterials, the high energy absorption capacity, reusable mechanical shock-absorbing, programmable mechanical behaviours and reconfigurability have been proposed and predicted theoretically.[11, 16, 17] Babaee *et al*. designed a group of 3D soft metamaterials via Bucklicrystals and theoretically revealed their buckling-induced auxetic effect.[16] The mechanical metamaterials are unlike conventional energy absorption materials via solid foam consisting of a pseudo-stochastic spatial arrangement of voids and constituent materials, which can lead to local structural heterogeneities and non-uniform properties. The deformation behaviours of metallic or plastic foams are usually not programmable so that the topological design of directional property is hard to achieve. However, there are few metamaterials with high performance of energy absorption in practical. For end-use applications, a critical challenge lies in

designing and fabricating such materials, in particular with desirable combinations of material formulation and spatial structures in multiscale.

3D printing or additive manufacturing (AM) offer the opportunity for the rational design and control of periodically patterned structures, and the topology of building blocks can realize their metabehaviours such as negative stiffness and negative Poisson's ratio. For example, Fang's group demonstrated the categories of lightweight 3D mechanical metamaterials with tunable negative thermal expansion[9] or ultrastiffness[12] due to the advanced microstereolithography with the capability of material digitalization in 3D. Frenzel *et al.* also designed and fabricated a 3D chiral microstructures with twist degrees of freedom going quantitatively beyond Cauchy elasticity.[8]

3D printing via selective laser sintering (SLS) has been employed to fabricate ceramic, metallic and polymeric composites with features ranging from microns to meters in sizes.[16, 18] The essence of this approach is the design of constituents and microstructures of feedstocks via composite powders that possess desirable flow capability and interaction with a laser source to allow the formation of the condensed bulk composite.[19, 20] The laser-sintered auxetic metamaterials may satisfy the following requirements for energy absorption: i) tough constituent materials, ii) flexible nodes or junctions in structures, iii) large volume deformation of structures upon compression, and iv) large-size manufacturing of structures. Meanwhile, SLS has the merits of supporting structureless, ease of post-treatment and cost-effective, as compared with other AM techniques requiring extra supporting structures or layouts and complicated post-treatment, such as selective laser melting (SLM), fused deposition modeling (FDM) and stereolithography (SLA).

The integration of the high-performance nanocomposite and desirable 3D structures would allow one both to exploit the structural advantages of auxetic metamaterials and reveal their potential of superior energy absorption. To implement this concept, we proposed laser sintering of

carbon nanotubes (CNTs) reinforced-nanocomposite powders to create the crystal-inspired 3D mechanical metamaterials with high performance in specific energy absorption, which goes beyond the conventional metallic stochastic foams or the previously reported 3D-printed composite and metallic lattices. As illustrated in **Figure 1**, this benchmark achievement of mechanical metamaterials arises from the engineerable 3D structures in a hierarchy. The constituent materials via nanocomposites exhibited the exceptional tensile toughness and specific energy absorption, due to the network of the CNTs toughening the continuous matrices. The producible topologies of structures are bending-dominated or buckling-dominated and behave in a highly compliant manner, which is strongly recommended for energy absorption. A construction is most efficient in energy dissipation when as many structural elements as possible are avoided to align with the loading direction while guaranteeing enough structural instability and force dissipation. These auxetic lattices are nearly isotropic and highly structural connectivity and showed negative Poisson's ratio and large geometric non-linearities upon a static compression.

Polyamides (PAs) are a good demonstration platform for current approach because the polyamide 11 and polyamide 12 occupy the 90% market share of printable thermoplastics in SLS. PA12 has widely reported properties tending to converge around a tensile strength of approximately 45 MPa and an elongation at break of 28%.[21] The stock powders (PA12) with an average particle size of 60 μm (Figure S3) were coated with a layer of surfactant functionalized CNTs using a latex technique, which ensures an uniform assembly of CNTs on a surface.[22] The systematic powder evaluation and process optimization for laser sintering process have been demonstrated in our previous works.[19, 21] The CNT-coated powders can effectively absorb laser energy to promote their melting-consolidation as well as the formation of the 3D continuous network within polymeric matrices. However, as a positive correlation exists between the

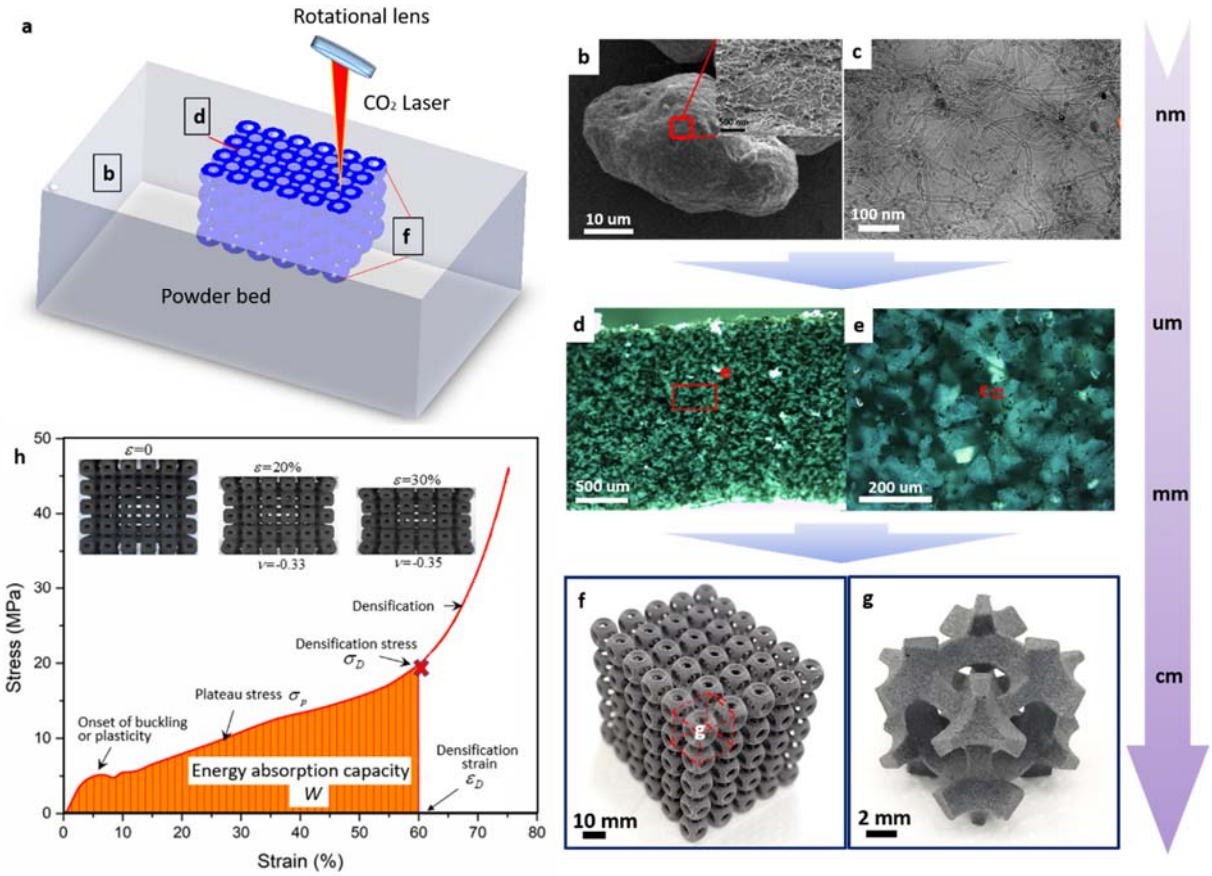

Figure 1. (a) Schematic illustration of a typical building platform for selective laser sintering (SLS) process. (b) The feedstock powder with a layer of CNT coating. (c) The networks of CNTs within sintered CNT/PA12 composites. (d) and (e) The microstructures of laser-sintered composite with different magnifications. (f) The laser-sintered composite metamaterials with BCC-6H pattern. (g) The representative cell unit of the BCC-6H lattice. (h) The energy-absorption performance of the BCC-6H lattice illustrated by the stress-strain curve. The critical transitions of mechanical deformation such as average plateau stress, densification strain and densification stress are indicated in the strain-stress curve.

thickness of the surface coating and the viscosity of melted composites, the increased melt viscosity caused by a thicker coating may induce a fusion barrier to prevent the powder consolidation within a short laser exposure. Therefore, the optimal loading ratio can be achieved when the coating layer can effectively enhance the energy absorption as well as retain the sufficiently low melt viscosity to ensure the rapid fusion of composite melt.[23]

To achieve the optimal mechanical performance of laser-sintered CNT/PA12 composite, the varied material combinations are applied in the SLS system. The CNTs with a diameter range of 20-40 nm or 40-60 nm are coated onto PA12 powders as stock feeding materials. In **Figure 2**a, the optimal CNT/PA12 composite exhibits significantly improved properties with the values of Young's modulus $E = 1301 \pm 14.5$ MPa, ultimate tensile strength $\sigma_u = 68 \pm 2.6$ MPa and elongation at break $\varepsilon_f = 33 \pm 4\%$, and these properties are nearly independent from the longitudinal and transverse building directions. To further investigate the isotropic strengthening and toughening mechanisms, the microstructure characterizations are conducted on the sintered composites and their deformed components. The observation reveals that the homogeneous 3D distribution of CNT-network can prohibit the movement of the segregated polymer phases and thus strengthen the matrix (Figure 2b, c). On the other hand, the microstructure of the deformed composite shows that the external force causes the large deformation of polymeric segments at microscale. The resulted CNTs-network is densely compacted and remains among the boundaries of those segments (Figure 2d, e). Such finely compacted microstructure provides a means to accommodate strain and thus prevents crack initiation and growth so as to toughen the matrix.[24] However, the increase of loading of CNTs (20-40 nm) to 1 wt.% adversely impacts on the mechanical properties of polymeric matrix (Figure 2a). The addition of CNTs (40-60 nm) of 0.5 wt.% also causes a drop of elongation at break from 28% to 24%. These observations are mainly because the increased coating layer raises the melt viscosity of composites and then prohibits the consolidation of melted powders. As a result, the insufficient fusion induces enormous microdefects or voids, leading to the brittle failures of sintered composites and the drawbacks of their ductility (Figure. S3). Therefore, the optimization of composite formulation and the effective control of sintering

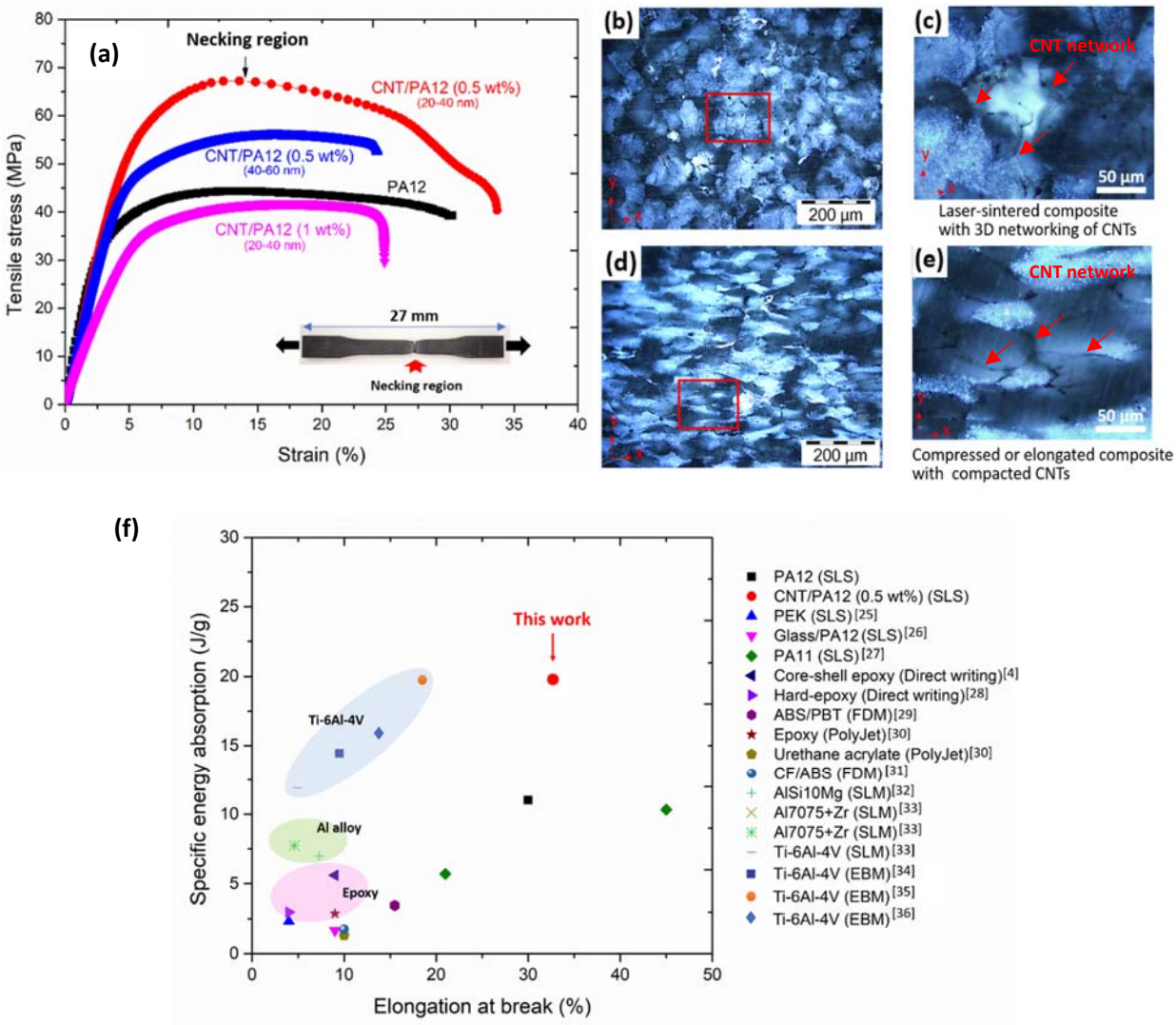

Figure 2. a) Tensile stress-strain curves of PA12 and CNT/PA12 with the weight percentages of 0.5% and 1%. Two sets of CNTs with the length range of 20-40 nm and 40-60 nm are selected. b) and c) The original microstructures of CNT within the polymeric matrix with different magnifications. d) and e) The microstructures of the compressed or elongated specimen of CNT/PA12 with different magnifications. f) The comparison diagram of specific energy absorption versus elongation at break for 3D printed lightweight materials.

process are crucial steps to instantaneously enhance the strength and toughness of the CNT-reinforced nanocomposite without sacrificing its Young's modulus.

The mechanical properties (e.g. toughness, specific energy absorption and ductility) of the optimized CNT-reinforced composites are not only superior to these of neat polymers but also

exceed these of many widely used 3D-printed materials including plastics, composites, and alloys (Figure 2f). To employ the CNT-reinforced powders for SLS process makes a pivotal contribution to engineering the desired composition and micro-architecture, resulting in the enhanced elongation at break of 33% and remarkable specific energy absorption of 20.68 J/g. The mechanical properties of available 3D-printed materials are summarized in Table S1. In comparison, the polymeric composites additively manufactured by FDM or direct writing usually have interfacial defects and inevitable cavities between polymer phases and microfibers.[28, 37] The aluminum and titanium alloys via SLM and electron beam melting (EBM) both exhibited a main drawback in their elongation at break, which are associated with the formation of unpredictable microdefects and strong residual stress during the rapid melting-consolidation.[23]

Further, to fabricate auxetic metamaterials via laser-sintering nanocomposite maybe an effective strategy to achieve a combination of advantageous mechanical performance rooting in constituent materials and structural geometry. The auxetic metamaterials consist of an array of patterned spherical shells namely building blocks, which can be arranged spatially to form crystal-mimic structures. The assembly of hollow spherical blocks in BCC pattern is highly compressible and deformable due to the high structural instability. The design of building block can be topologically optimized by varying the geometry of the shell thickness, the number of holes and the angle of projection as shown in Figure S5. It is crucial to understand the fundamental relationships between geometry, mechanical properties, and deformation mechanisms in order to engineer the allowable compressive stress and optimal energy absorption capacity of auxetic lattices.

To determine the effect of 3D architectures on energy absorption performance, 6-hole and 12-hole building blocks are selected to assemble the BCC pattern and the shell thickness are tailored

to change the absolute density and relative density of auxetic lattices to be 100-301 kg/m^3 and 0.09-0.3, respectively (**Figure 3**a). This density range is comparable to that of aerogel, alumina nanolattices and other ultralight materials.[14, 15, 38] The compressive stress-strain curves reveal the deformation and energy absorption behaviours upon the quasi-static compressions (**Figure 3**d, e). The failure mechanisms govern the deformation behaviours; the competing failure mechanisms exist for composite auxetic lattices: fracture of the material, node yielding, global (Euler) buckling of the connected unit and local (shell) buckling of individual building block. Buckling always occurs at a lower stress than the material fractures. Different transitions of failure mechanisms can occur during deformation, depending on the stress state that arises in the spherical shells and rotational nodes during loading.

For the BCC-6H pattern, the lattice ($\rho^* > 20$ %) are elastically deformed to reach the onset of buckling or plasticity and then its compressive stresses increase slowly within the stress plateau region due to global buckling and post-yielding (Fig. 3d). The entire lattice undergoes a large effective compressive strain due to the extensive rotations of ligaments around the connective nodes. This buckling-induced rotation is revealed by finite element analysis of elastic-buckling and post-buckling effects (Figure. S8). With reducing shell thickness of building block ($\rho^* <$ 20 %), the failure mechanism shifts to local buckling-dominated behaviours (Figure S13). The progressive deformation via discrete layer-by-layer fractures is revealed by the fluctuation of stress-strain curve in a broad plateau (Figure 3d).

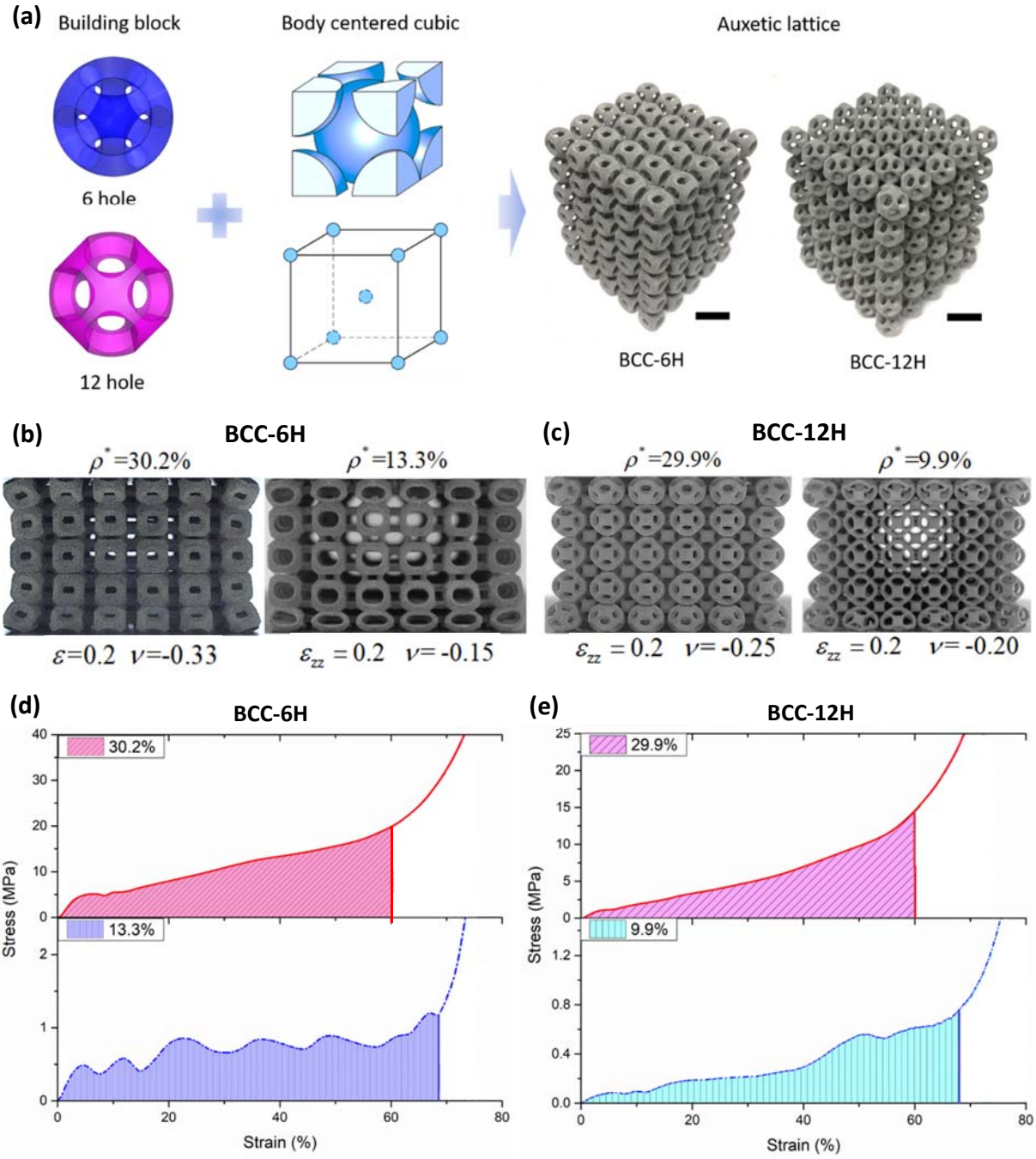

Figure 3. a) Illustration of the concept of structural designs of BCC-6H and BCC-12H metamaterials. (Scale bar is 10 mm) b) and c) The structural deformations of auxetic BCC-6H and BCC-12H lattices with respect to the different relative densities. d) and e) The compressive stress-strain curves of BCC-6H and BCC-12H lattices with respect to the different relative densities. The coloured-areas under curves indicate the energy absorbed by structures during the quasi-static compressions.

For the BCC-12H pattern, the compressive stress shows a nearly linear relationship with strain until the densification strain. It is observed that the auxetic lattices endow with a significant strain hardening effect crossing the range of relative density from 9.9% to 33% (Figure S9). The FE simulation reveals the deformation evolution of representative unit of BCC-12H, the global buckling is dominating to induce the notational rotation as well as the segmental rotation within the individual unit cell (Figure. S8). The competing failure mechanisms for BCC-12H structures include global buckling, node yielding and local fracture of the unit cell. The transitions between each two deformation modes is usually driven by an energetic competition between structural buckling and material failure. To predict the stresses necessary to initiate each individual failure mechanism, the regions of stress concentration and strain localization are demonstrated in the largely deformed representative unit. In Figure 3c, once the nodes are relieved with cracks, the failure model transits from the global buckling to the excessively localized fracture in a unit cell as the shell thickness approaches to the critically thin level. In short, we found that the global buckling effect is the dominated mechanism to induce the auxetic behaviour of the crystal-inspired hollow lattices. In Figure 3b, c, the BCC-6H lattice with relative high density shows much critical negative Poisson's ratio effect as compared with others, therefore, it withstands the largest volume reduction upon compression to universally dissipate mechanical energy, which reveals its potential of effective energy absorption.

The classical foam theory allows detections of the governing failure mechanism, applying the according relations of Gibson and Ashby.[39] In **Figure 4**a, b, the normalized energy absorption per unit volume W / E_s for auxetic composites are plotted corresponding to the normalized peak stress σ_p / E_s . These diagrams are the effective guidance of material selection for energy absorption with the customizable stress level and programmable energy absorption capacity for

the specific application. The optimum structure for a given category is the one that absorbs the most energy up to the maximum permitted compressive stress σ_{p}. Each lattice density has a σ_{p} corresponding to the shoulder on the energy curve. Thereafter, the optimum energy absorption follows the envelope of the individual W-σ_{p} curves. For a foam structure, the energy absorption capacity can be expressed as a function of the densification stress σ_D and the relative density of structure [39]

$$\frac{W_{\max}}{E_{\mathrm{s}}} = \mathrm{A}\left(\frac{\sigma_D}{E_{\mathrm{s}}}\right)^{\alpha}\left(\frac{\rho}{\rho_{\mathrm{s}}}\right)^{\beta}, \text{ at } \varepsilon=\varepsilon_{\mathrm{D}} \tag{1}$$

where A, E_{s}, ρ_{s}, ρ and ε_{D} are an empirical parameter, the Young's modulus, the density of constituent material, the density of lattice and the densification strain of lattice, respectively.

In **Figure 4**a, b, the envelope as a linear function can be expressed as

$$\frac{W_{\max}}{E_{\mathrm{s}}} = \mathrm{B}\left(\frac{\sigma_{\mathrm{D}}}{E_{\mathrm{s}}}\right)^{\eta}, \text{ at } \varepsilon=\varepsilon_{\mathrm{D}} \tag{2}$$

The value of η indicates the slope of the envelope, which connects the shoulders at each $\sigma_{\mathrm{p}} = \sigma_D$ correspondingly to the auxetic composites with varied relative densities. The BCC-12H lattices follow the power law scaling with the densification stress as the slope η=1.01. This is similar to the bending- and buckling-dominated open-cell elastomeric stochastic foam with $\eta \approx 1$ at low stresses.[40] Nevertheless, the BCC-6H lattices with $\eta \approx 0.78$ exhibit a slightly degraded trend of the incremental ΔW, as the densification stress increases by several orders of magnitude.

Meanwhile, the $\frac{\sigma_D}{E_s}$ value of a porous material scales linearly or exponentially with its relative density $\rho^*=\frac{\rho}{\rho_s}$.[14] The optimal value of energy absorption capacity W_{max} follows the scaling law given by

$$\frac{W_{max}}{E_s} = C(\rho^*)^{\gamma}, \quad (3)$$

The BCC-6H and BCC-12H auxetic lattices are demonstrated with the scaling factor γ of 3 and 5/2, respectively. In comparison, these groups of auxetic composites exhibit relatively higher scaling factors than the elastomeric and plastic stochastic foams with the value of 2 and 3/2, respectively.[39] These auxetic lattices are highly isotropic so that the relationship of energy absorption capacity with lattice density does not vary with the orientation of the printed lattice composites, as confirmed by compressing lattices along different loading directions (Figure S11, S12). Especially, the BCC-6H lattices exhibit the remarkable scaling relationship (γ=3), which indicates the effective increment of energy absorption as the lattice density slightly increases. As compared with the stochastic foam with random porous distribution, each representative unit of the auxetic composite experiences the large volume deformation and shrinks isotopically, inducing the universal volume shrinkage to effectively absorb the external energy. In fact, the energy absorption capacity of the auxetic structure also outperforms that of traditional structural lattices such as honeycomb (In-plane), octet-truss and pyramidal lattices (Figure S14). This is because the bending-dominated or stretching-dominated truss lattices cannot deform universally to sustain large compressive strain due to their localized strut fractures or structural collapses.[12]

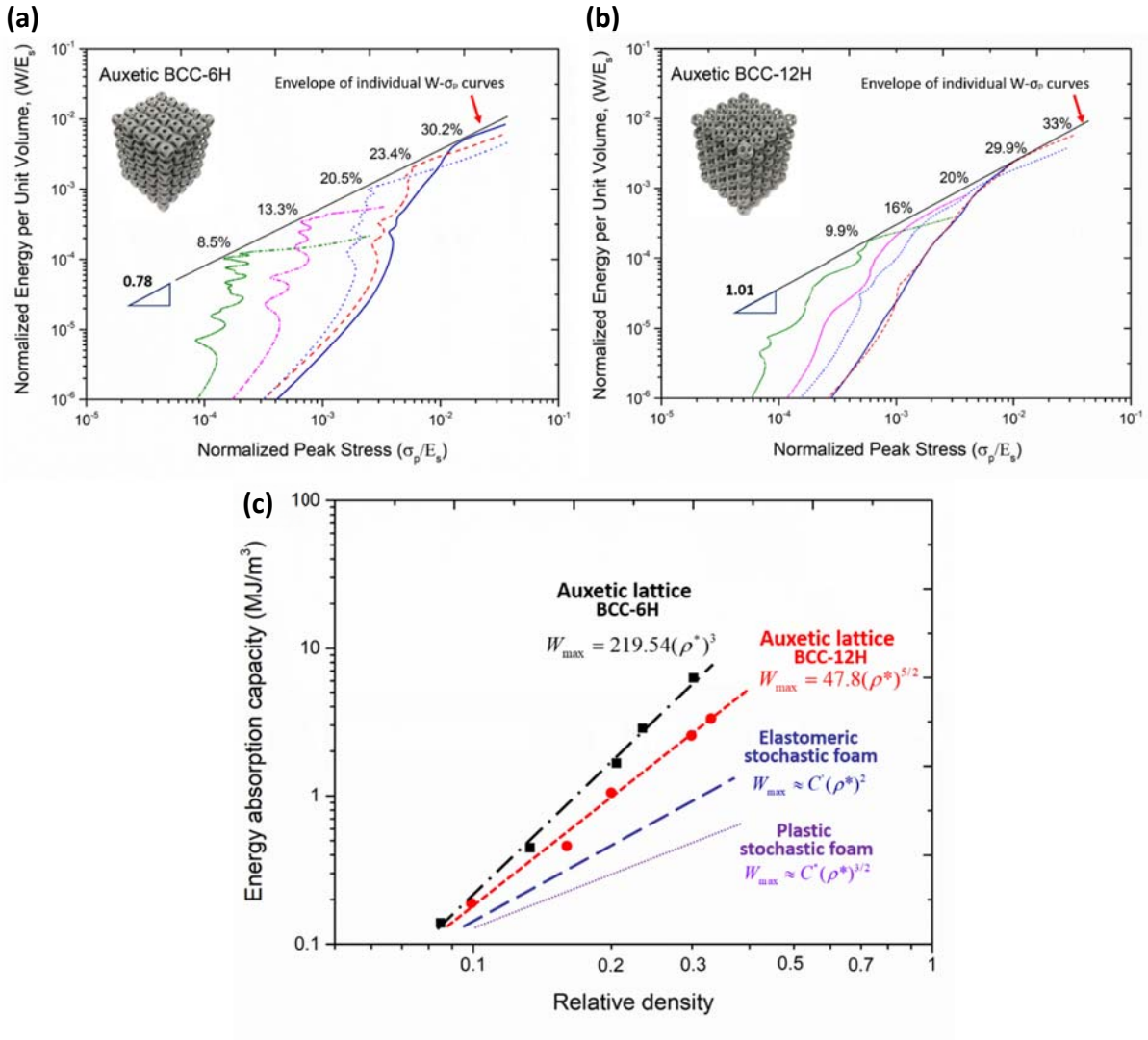

Figure 4. Energy absorption performances of auxetic lattices. a) and b) the energy absorption diagrams of auxetic BCC-6H and BCC-12H lattices with the energy absorbed per unit volume against peak stress generated by external compression or impact. Both axes are normalized by the solid modulus. The envelope which just touches each curve defines the optimum choice of foam at the specific strain-rate, c) the relationships of energy absorption capacity versus relative density for auxetic lattices ($\rho^* \geq 10\%$) as compared with the elastomeric and plastic stochastic foams.

This work account for the observed ductile-like behavior of the auxetic lattices and non-linearly plastically deformed structures composed of intrinsically tough nanocomposite are virtually explored. Up to densification strain, the BCC-6H and BCC-12H auxetic lattices exhibit excellent energy absorption capacity within the ranges of 0.13-6.29 and 0.18-2.55 MJ/m^3,

respectively. These auxetic lattices have the remarkable specific energy absorption of W_{max}/ρ ranging from 1.6 J/g to 20.42 J/g, which is comparable with that of the nickel, alumina nanolattices and titanium alloy structures and goes beyond that of normal aluminum alloy foams and other 3D-printed structures as shown in **Figure 4**.[2, 40] In comparison, the lightweight titanium foams exhibit the outstanding performance, nevertheless, their manufacturing approaches (e.g. EBM, SLM and laser cladding) are expensive and high energy consumption as compared with current approach for lightweight composite fabrication. To date, microstereolithography and direct writing techniques are still limited by their building sizes to achieve large-size structures. In fact, laser-sintered auxetic composites possess the advantages of excellent specific energy absorption and economic efficiency in the end-use applications such as automobile and aerospace industries.

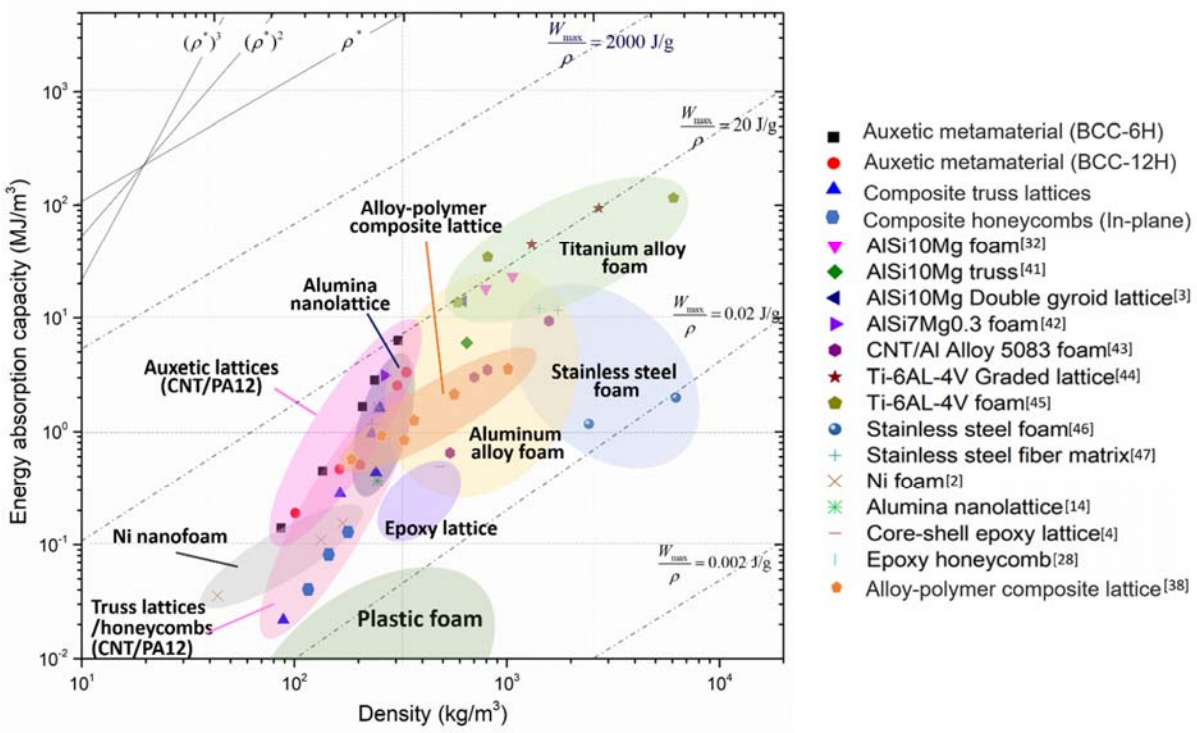

Figure 5. Ashby map of energy absorption per unit volume versus density. This chart compares auxetic metamaterials against other most advanced metallic and composite structures so far. (Note: the summary of material data sources is provided in the SI.)

We displayed the creation of buckling-dominated auxetic metamaterials via SLS. These metamaterials achieve the programmable shape transformation and remarkable energy absorption capability through effectively combining the material design and the structure selection. The energy absorption performance of laser-sintered nanocomposite metamaterials depends on both the deformation mechanism of the structural ligaments, which buckle under compression at relatively low strains, and the microstructure of constituent materials. The integration of high-performance nanocomposite and mimic-crystal auxetic design using 3D printing technique provides an insightful perspective on advanced manufacturing for the applications as a cushion, impact protection, explosion-proof, protective packaging, etc. The 3D-printed nanocomposite metamaterials offer attractive alternatives to stochastic plastic and metallic foams because of their auxetic deformation, programmable behaviour, high predictability and excellent energy absorption capability, with a large potential in highly value-added industries such as aerospace and military.

Experimental Section

Process for composite powder development: The composite powder CNT/PA12 was prepared through a surfactant-facilitated latex technique. Under atmospheric pressure, PA12 powders (PA2200 from EOS GmbH, Krailling, Germany) and the solution of multi-walled CNTs with the diameter of 20-40 nm or 40-60 nm and the length of >5 μm (Hangzhou Corker Composite Material Co. Ltd. China) were mixed in the heated aqueous suspension at 90°C for 1 hour and then cooled down to room temperature. The powders adsorbed with CNTs could precipitate out for further filtration and drying. Sodium cholate hydrate (BioXtra, ≥ 99%, Sigma-Aldrich) was used as a surfactant to modify the MWCNTs in the deionized water before the composite preparation. The composition of composite powders was varied by tuning the weight ratio of multi-walled CNTs.

3D Printing via Selective laser sintering: All laser-sintered composite materials and structures were accomplished with selective laser sintering (EOSP395, Germany) equipped with a CO_2 laser ($\lambda = 10.6$ μm, laser power up to 50W). The parameters including laser scanning speed, laser powder, layer thickness and hatching space were considered to optimize the mechanical performances of the sintered composite materials. The optimized process parameters were followed by the commercial PA12 parameter set from EOS P395 system. Processing was completed after the processing chamber was cooled down to room temperature. The specimens were removed from the machine and cleaned of extra powder by sandblasting and cleaned by compressed air. The tensile and compressive specimens are printed following the ASTM standard (D638 14) and (D695 15), respectively. The cubic specimens (15mm × 20mm × 25mm) were polished for examining microstructure.

Mechanical evaluation: The tensile and compressive properties of the sintered composites were measured using an Instron 3360 load frame (Instron, Norwood, MA) The tensile and

compression rate applied on the specimens were 2 mm/min and 0.5~4 mm/min, respectively. The specific tensile toughness of each material U_T is described as equation

$$U_T = \frac{1}{\rho_s}\int_0^{\varepsilon_d} \sigma(\varepsilon) d\varepsilon \,, \tag{1}$$

where the $\sigma(\varepsilon)$ is the tensile stress corresponding to strain and ε_d is elongation at break; ρ_s is the density of laser-sintered composite.

Compression tests of the auxetic lattices were conducted on an Instron 3343 Universal testing machine with 10 kN load cell and the applied normal strain was fixed at an identical displacement rate of 6 mm/min. The tensile properties of specimens are an average value. The energy absorption capacity of each lattice W (MJ/m^3) is given by equation

$$W = \int_0^{\varepsilon} \sigma(\varepsilon) d\varepsilon, \quad (0 \le \varepsilon \le \varepsilon_D) \tag{2}$$

where ε_D is the densification strain of each lattice upon compression and identified at the strain with maximum absorption efficiency of a structure E_{max} given by equation

$$E_{max} = \frac{1}{\sigma\,\varepsilon}\int_0^{\varepsilon} \sigma(\varepsilon) d\varepsilon \,, \tag{3}$$

where σ_D and ε_D can be obtained when E_{max} is achieved. Thereafter the optimal value of energy absorption per mass via specific energy absorption U_{max} as described by equation

$$U_{max} = \frac{W_{max}}{\rho} = \frac{1}{\rho}\int_0^{\varepsilon_D} \sigma(\varepsilon) d\varepsilon \,, \tag{4}$$

where W_{max} is the maximum energy absorption of lattice upon compression via energy absorption capacity, and ρ is the lattice density.

Characterizations: To characterize the surface morphologies and microstructures of composite powders, a field emission scanning electron microscope (FE-SEM) (JSM-7600F, Tokyo, Japan)

was employed with an electron beam voltage of 2~5 kV. To capture the microstructure using an optical microscope (Olympus DP72, MA, 02453, USA), the CNT/PA12 samples were required to be well polished for the optical characterization.

Supporting Information

Supporting Information is available from the Wiley Online Library or from the author.

Acknowledgement

The authors would like to acknowledge the financial support from the National Research Foundation Medium Sized Center, Singapore through the Marine and Offshore Program and the Ministry of Education, Singapore (Academic Research Fund, TIER 1-RG174/15).

Reference

[1] Y. Chen, T. Li, Z. Jia, F. Scarpa, C. W. Yao, L. Wang, *Materials & Design* **2018**, 137, 226; M. Mohsenizadeh, F. Gasbarri, M. Munther, A. Beheshti, K. Davami, *Materials & Design* **2018**, 139, 521.

[2] S. Fan, T. Zhang, K. Yu, H. Fang, H. Xiong, Y. Dai, J. Ma, D. Jiang, H. Zhu, *Transactions of Nonferrous Metals Society of China* **2017**, 27, 117.

[3] I. Maskery, N. T. Aboulkhair, A. O. Aremu, C. J. Tuck, I. A. Ashcroft, *Addit. Manuf.* **2017**, 16, 24.

[4] J. Mueller, J. R. Raney, K. Shea, J. A. Lewis, *Adv. Mater.* **2018**, 1705001.

[5] S. Kruk, Y. Kivshar, *ACS Photonics* **2017**, 4, 2638.

[6] T. Brunet, J. Leng, O. Mondain-Monval, *Science* **2013**, 342, 323.

[7] M. H. Lu, L. Feng, Y. F. Chen, *Mater. Today* **2009**, 12, 34.

[8] T. Frenzel, M. Kadic, M. Wegener, *Science* **2017**, 358, 1072.

[9] Q. Wang, J. A. Jackson, Q. Ge, J. B. Hopkins, C. M. Spadaccini, N. X. Fang, *Phys. Rev. Lett.* **2016**, 117, 175901.

[10] G. M. Akselrod, C. Argyropoulos, T. B. Hoang, C. Ciracì, C. Fang, J. Huang, D. R. Smith, M. H. Mikkelsen, *Nat. Photonics* **2014**, 8, 835.

[11] S. Babaee, J. Shim, J. C. Weaver, E. R. Chen, N. Patel, K. Bertoldi, *Adv. Mater.* **2013**, 25, 5044.

[12] X. Zheng, H. Lee, T. H. Weisgraber, M. Shusteff, J. DeOtte, E. B. Duoss, J. D. Kuntz, M. M. Biener, Q. Ge, J. A. Jackson, S. O. Kucheyev, N. X. Fang, C. M. Spadaccini, *Science* **2014**, 344, 1373.

[13] R. H. Baughman, *Nature* **2003**, 425, 667; G. N. Greaves, A. L. Greer, R. S. Lakes, T. Rouxel, *Nat. Mater.* **2011**, 10, 823.

[14] L. R. Meza, S. Das, J. R. Greer, *Science* **2014**, 345, 1322.

[15] J. Bauer, A. Schroer, R. Schwaiger, O. Kraft, *Nat. Mater.* **2016**, 15, 438.

[16] S. Yuan, F. Shen, J. Bai, C. K. Chua, J. Wei, K. Zhou, *Mater. Des.* **2017**, 120, 317.

[17] E. B. Duoss, T. H. Weisgraber, K. Hearon, C. Zhu, W. Small, T. R. Metz, J. J. Vericella, H. D. Barth, J. D. Kuntz, R. S. Maxwell, C. M. Spadaccini, T. S. Wilson, *Adv. Funct. Mater.* **2014**, 24, 4905.

[18] S. Cijun, G. Chengde, N. Yi, H. Huanlong, Z. Ying, P. Shuping, *Nanotechnology* **2011**, 22, 285703.

[19] F. Shen, S. Yuan, C. K. Chua, K. Zhou, *J. Mater. Process. Technol.* **2018**, 254, 52.

[20] X. Tian, G. Peng, M. Yan, S. He, R. Yao, *Int. J. Heat Mass Transfer* **2018**, 120, 379.

[21] S. Yuan, J. Bai, C. Chua, J. Wei, K. Zhou, *Polymers* **2016**, 8, 370.

[22] S. Yuan, J. Bai, C. K. Chua, J. Wei, K. Zhou, *Composites Part A* **2016**, 90, 699.

[23] W. Yan, W. Ge, Y. Qian, S. Lin, B. Zhou, W. K. Liu, F. Lin, G. J. Wagner, *Acta Mater.* **2017**, 134, 324.

[24] H. D. Wagner, R. A. Vaia, *Materials Today* **2004**, 7, 38; D. R. Paul, L. M. Robeson, *Polymer* **2008**, 49, 3187.

[25] O. Ghita, E. James, R. Davies, S. Berretta, B. Singh, S. Flint, K. E. Evans, *Mater. Des.* **2014**, 61, 124.

[26] S. Gaikwad, J. S. Tate, N. Theodoropoulou, J. H. Koo, *J. Compos. Mater.* **2012**, 47, 2973.

[27] J. Bai, S. Yuan, F. Shen, B. Zhang, C. K. Chua, K. Zhou, J. Wei, *Virtual Phys Prototyp.* **2017**, 12, 235.

[28] B. G. Compton, J. A. Lewis, *Adv. Mater.* **2014**, 26, 5930.

[29] (Ed: S. A. d. P. ABS_Black).

[30] Y. Mao, Z. Ding, C. Yuan, S. Ai, M. Isakov, J. Wu, T. Wang, M. L. Dunn, H. J. Qi, *Sci. Rep.* **2016**, 6, 24761.

[31] N. Fuda, C. Weilong, H. Yingbin, W. Hui, *J. Compos. Mater.* **2016**, 51, 451.

[32] L. Stanev, B. Drenchev, A. Yotov, R. Lazarova, *J. Mater. Sci. Technol.* **2014**, 22, 9.

[33] J. H. Martin, B. D. Yahata, J. M. Hundley, J. A. Mayer, T. A. Schaedler, T. M. Pollock, *Nature* **2017**, 549, 365.

[34] H. K. Rafi, N. V. Karthik, H. Gong, T. L. Starr, B. E. Stucker, *J. Mater. Eng. Perform.* **2013**, 22, 3872.

[35] L. E. Murr, S. M. Gaytan, D. A. Ramirez, E. Martinez, J. Hernandez, K. N. Amato, P. W. Shindo, F. R. Medina, R. B. Wicker, *J. Mater. Sci. Technol.* **2012**, 28, 1.

[36] J. Parthasarathy, B. Starly, S. Raman, A. Christensen, *J. Mech. Behav. Biomed. Mater.* **2010**, 3, 249.

[37] F. Ning, W. Cong, Y. Hu, H. Wang, *J. Compos. Mater.* **2017**, 51, 451; N. Mohan, P. Senthil, S. Vinodh, N. Jayanth, *Virtual Phys Prototyp.* **2017**, 12, 47; J. P. Lewicki, J. N. Rodriguez, C. Zhu, M. A. Worsley, A. S. Wu, Y. Kanarska, J. D. Horn, E. B. Duoss, J. M. Ortega, W. Elmer, R. Hensleigh, R. A. Fellini, M. J. King, *Sci. Rep.* **2017**, 7, 43401; J. R. Raney, B. G. Compton, J. Mueller, T. J. Ober, K. Shea, J. A. Lewis, *Proceedings of the National Academy of Sciences* **2018**.

[38] X. Zhang, J. Yao, B. Liu, J. Yan, L. Lu, Y. Li, H. Gao, X. Li, *Nano Lett.* **2018**, 18, 4247.

[39] L. J. Gibson, M. F. Ashby, *Cellular Solids: Structure and Properties*, Cambridge University Press, Cambridge **1997**.

[40] G. Lu, T. Yu, in *Energy Absorption of Structures and Materials*, Woodhead Publishing, **2003**, 268.

[41] I. Maskery, N. T. Aboulkhair, A. O. Aremu, C. J. Tuck, I. A. Ashcroft, R. D. Wildman, R. J. M. Hague, *Mater. Sci. Eng. A* **2016**, 670, 264.

[42] A. Jung, H. Natter, S. Diebels, E. Lach, R. Hempelmann, *Adv. Eng. Mater.* **2010**, 13, 5.

[43] A. Aldoshan, S. Khanna, *Mater. Sci. Eng. A* **2017**, 689, 17.

[44] S. Y. Choy, C. N. Sun, K. F. Leong, J. Wei, *Mater. Des.* **2017**, 131, 112.

[45] B. Xie, Y. Z. Fan, T. Z. Mu, B. Deng, *Mater. Sci. Eng. A* **2017**, 708, 419.

[46] A. T. Youness, R. Afsaneh, *Procedia Mater. Sci.* **2014**, 4, 377.

[47] J. C. Qiao, Z. P. Xi, H. P. Tang, J. Y. Wang, J. L. Zhu, *Mater. Trans.* **2008**, 49, 2919.